Atmos. Meas. Tech., 19, 7097–7112, 2026
https://doi.org/10.5194/amt-19-7097-2026
© Author(s) 2026. This work is distributed under
the Creative Commons Attribution 4.0 License.

Atmospheric Measurement Techniques
Open Access
EGU

# Calculation of the impacts of aerosols on cloud microphysical properties by combining ground- and space-based measurements

**Suzanne Crumeyrolle[1], Quentin Coopman[1], Eric Bourrianne[1], Clara Lapointe[1], Eloise Delbarre[1], Elise Devigne[1], Olivier Pujol[1,2], Romain De Filippi[1], and Timothy J. Garrett[3]**

[1]Univ. Lille, CNRS, UMR 8518 – LOA – Laboratoire d'Optique Atmosphérique, 59000 Lille, France
[2]Institut Universitaire de France (IUF), Maison des Universités, 75005 Paris, France
[3]Department of Atmospheric Sciences, University of Utah, Salt Lake City, UT 84112, USA

**Correspondence:** Suzanne Crumeyrolle (suzanne.crumeyrolle@univ-lille.fr)

Received: 6 February 2026 – Discussion started: 28 April 2026
Revised: 24 September 2026 – Accepted: 2 October 2026 – Published: 6 November 2026

**Abstract.** The effect of aerosols on cloud properties remains poorly constrained, in part because ground-based measurements are highly local while space-based retrievals are spatially imprecise representing averages over large footprints. Here, we show how the two viewpoints can be combined using colocated surface aerosol measurements and thermodynamic profiling from the peri-urban ATOLL (ATmospheric Observatory in LiLLe) site and geostationary-satellite cloud microphysical retrievals from the SEVIRI instrument. Focusing on low-level shallow clouds that formed under thermodynamically stable conditions, we relate cloud properties to aerosol light scattering as a proxy for cloud condensation nucleus concentrations for two cloud liquid water path bins of 20–100 and 100–200 $\mathrm{g\,m^{-2}}$. Relative changes of cloud droplet number concentrations and effective radii are compared to relative changes in aerosol light scattering coefficient to find respective susceptibilities. The susceptibility of the cloud droplet number concentration to the aerosol scattering coefficient ($S_\mathrm{n}$), also called the nucleation efficiency, is found to be approximately 0.4 for liquid water path (LWP) values between 20 to 100 $\mathrm{g\,m^{-2}}$ and approximately 0.33 for LWP ranging from 100 to 200 $\mathrm{g\,m^{-2}}$. For the same LWP ranges, the susceptibility of the effective radius to the aerosol burden ($S_\mathrm{re}$) is approximately 0.12 and 0.08, respectively. These values are consistent with, although on the lower side of, prior studies of continental stratus. Uncertainties in this study are dominated by a small sample size and satellite retrieval biases. However, the approach can be readily extended to other ground-based sites measuring boundary layer aerosol concentrations, and so our study offers a method for better constraining susceptibility calculations globally.

## 1 Introduction

The fact that radiative properties of clouds respond to aerosols is no longer in question (Boucher et al., 2013). The magnitude of aerosol-cloud interactions (ACI), however, remains among the largest sources of uncertainty in Earth's radiative budget (Quaas et al., 2009, Bellouin et al., 2020; Watson-Parris and Smith, 2022; Michibata, 2022; Duran et al., 2025) due to the complexity of atmospheric processes as well as observational limitations (Fan et al., 2016). Current assessments suggest uncertainties of more than $\pm 1\,\mathrm{W\,m^{-2}}$, comparable in magnitude to the estimated forcing itself (Bellouin et al., 2020; Forster et al., 2021).

Ground, satellite, and in-situ measurements have been used to estimate the susceptibility of cloud properties to aerosol burden. Satellite measurements of those susceptibilities have the advantage of being nearly global in scope, as well as observing the tops of clouds–the part that most directly reflects incoming solar radiation and is therefore most relevant to Earth's energy budget. However, such studies can be limited by how cloud moisture and reflected radiation contaminate retrievals of adjoining aerosol fields, as well as by the range of assumptions embedded in the retrieval algorithms of cloud liquid water path, droplet number concentration and diameter (Grosvenor et al., 2018; Jia et al., 2021). Because clouds are bright, it is not possible to simultaneously

observe from space aerosol properties directly below them, which is where their concentrations are most relevant for modifying boundary layer clouds (Gryspeerdt et al., 2016; Jia et al., 2021). Moreover, even in adjacent air, retrievals of aerosol optical depth (AOD) or aerosol index (AI) lack vertical resolution, and so they may include aerosols located at heights different from those that directly impact the observed clouds, e.g. the free troposphere rather than the boundary layer (Quaas et al., 2020).

Quaas et al. (2020) argue that in situ and ground-based measurements are better suited for quantifying relevant processes that remain poorly constrained by satellite observations, particularly finer scale processes such as air parcel updraft variability and aerosol spatial inhomogeneity. Airborne studies can capture cloud details, but are unsuitable for long term monitoring. Ground-based measurements can excel at measuring changes in aerosol concentration and chemistry, as well as boundary layer thermodynamic structure (Rosenfeld et al., 2014; Sena et al., 2016), but only few long-term ground-based sites exist that are capable of monitoring both aerosols and clouds. Even then, their insights are necessarily local, with uncertain global generality (McComiskey et al., 2009; Sarna and Russchenberg, 2016). Similarly, ground-based stations may measure a wide range of radiatively relevant cloud parameters using remote sensing instruments (McComiskey et al., 2009; Madhavan et al., 2012; Kim et al., 2012; Garrett and Zhao, 2013; Sarna and Russchenberg, 2016; Sena et al., 2016; Qiu et al., 2017; Zheng et al., 2020), but they are inherently limited by their temporal and geographical location.

In this study, we leverage a comprehensive dataset combining in-situ and remote sensing observations from both ground-based and satellite platforms to investigate aerosol-cloud interactions over the 2020–2024 period. While the combination of ground-based and satellite observations is not new, the novelty of this work lies in the framework developed to derive aerosol-cloud susceptibilities from coordinated ACTRIS (The Aerosol, Clouds and Trace Gases Research Infrastructure) aerosol measurements and geostationary satellite cloud retrievals under carefully constrained meteorological conditions. We demonstrate how cloud droplet concentration and effective radius susceptibilities to aerosol burden can be calculated by combining detailed in-situ aerosol observations obtained from a ground station with cloud microphysical properties retrieved from space (Lihavainen et al., 2010; Nandan et al., 2022). This approach exploits the complementarity of the two observing systems: ground-based measurements provide robust aerosol characterization under cloudy conditions, while geostationary satellite observations provide temporally resolved cloud microphysical retrievals from a top-down perspective. By linking both datasets in space and time, susceptibility estimates can be derived under well-constrained observational conditions. Moreover, by applying the methodology to a single, well-characterized site, we explore its strengths, limitations, and underlying assumptions. The broader objective is to lay the groundwork for future applications across a network of sites, rather than to draw generalized conclusions from the present analysis. Such an extension would take advantage of the advanced aerosol measurements available within ACTRIS, including aerosol chemical composition, enabling future investigations of aerosol-cloud susceptibilities as a function of aerosol type and composition.

## 2 Materials

The observational dataset used in this study covers the 2020–2024 period and combines complementary in-situ and remote sensing measurements acquired from ground-based and satellite platforms (Table 1). The instruments and datasets contributing to this observational framework are described in the following sections.

### 2.1 Ground based Measurements

The ATOLL observatory (50.6114° N, 3.1406° E; 19 m above ground level), shown in Fig. 1, operates within the ACTRIS framework (https://www.actris.eu/, last access: 8 October 2026) and is located in Villeneuve d'Ascq, a suburban area situated a few kilometers from the city of Lille, the central core of a densely populated metropolitan region. The surrounding environment is characterized by a mix of emission sources including traffic, residential heating, agricultural practices, industrial activities, and contributions from maritime transport (Chen et al., 2022). Measurements reported at this site (Velazquez-Garcia et al., 2023) highlight aerosol properties consistent with those typically observed in urban conditions, as defined within the GAW classification scheme (Laj et al., 2020; Rose et al., 2021). In addition to local influences, the site occasionally experiences the impact of air masses transported over long distances, bringing in particles associated with volcanic activity or Saharan dust events (Mortier et al., 2013; Bovchaliuk et al., 2016; Boichu et al., 2019).

#### 2.1.1 In situ measurements

The analysis presented here relies on observations collected between 2020 and 2024. Aerosol sampling was conducted through individual stainless-steel lines, each positioned one meter above the rooftop to limit microscale interferences. Depending on the instrument, the inlets were fitted with either $PM_1$ or $PM_{10}$ size-selective devices. Downstream the inlets, Nafion™ membranes were operated to keep relative humidity below 40 %, following ACTRIS guidelines.

Particle number size distributions spanning diameters from 10 to 800 nm were obtained with a time resolution of 5 min using a Scanning Mobility Particle Sizer (SMPS). The system combined a differential mobility analyzer (DMA, TSI 3082; Villani et al., 2007), a Ni-63 neutralizer (95 MBq), and

**Table 1.** Cloud and Aerosol Properties Measured or Derived from Observations at ATOLL, France.

| Measured parameter | Acronym (SI unit) | Instrument and algorithm | Citation |
|---|---|---|---|
| Cloud droplet number concentration | $n_d$ ($cm^{-3}$) | SEVIRI/CLAAS3 | Benas et al. (2023), Bennartz and Rausch (2017) |
| Cloud droplet effective radius | $r_e$ (µm) | SEVIRI/CLAAS3 | Benas et al. (2023), Nakajima and King (1990) |
| Total aerosol light scattering coefficient | $\sigma_{sp}$ ($Mm^{-1}$) | AURORA 4000 | Müller et al. (2009, 2011) |
| Condensation nuclei | CN ($cm^{-3}$) | SMPS | Villani et al. (2007) |
| Temperature and relative humidity profiles | $T$ (K) and RH (%) | MWRP | Cimini et al. (2004) |
| Boundary layer height | BLH (km) | MWRP | Sinclair et al. (2022) |
| Cloud liquid water path | LWP ($g\,m^{-2}$) | MWRP | Stephens (1978) |
| Cloud top and cloud base | CT and CB (km) | MWRP | Mascaut et al. (2022, 2023a, b) |

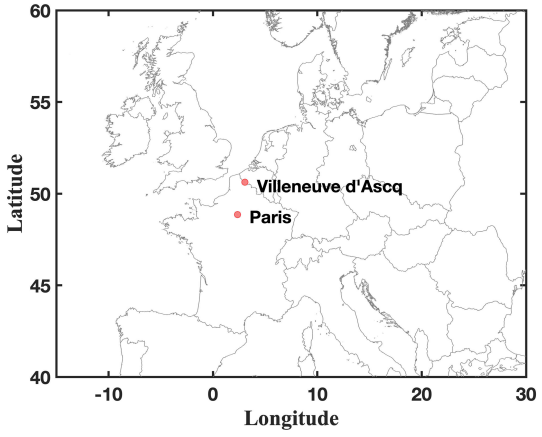



**Figure 1.** Geographic location (50.6114° N, 3.1406° E) of the ATOLL station in Villeneuve d'Ascq (northern France).

a condensation particle counter, initially a TSI 3775 and later replaced by a TSI 3750 (from May 2022). Instrumental configuration evolved slightly over time, notably with a reduction of the lower detectable particle diameter from 15.7 to 10 nm beginning in May 2022. Airflow conditions within the SMPS were maintained via a closed-loop arrangement regulated by a critical orifice (Jokinen and Mäkelä, 1997). Each measurement cycle lasted 300 s. Corrections applied during data processing included adjustments for particle charging probabilities and diffusional losses, implemented with the AIM software (version 10.2.0.11). To ensure robustness, integrated particle concentrations derived from the SMPS were regularly checked against an independent condensation particle counter (TSI 3775 and later TSI 3750).

Aerosol optical properties were derived from measurements of total and backscattering coefficients under dry conditions. For this purpose, two nephelometers (Aurora 4000 and Aurora 3000, Ecotech) operating at 450, 525, and 635 nm were deployed (Müller et al., 2009, 2011). The configuration allowed sequential characterisation of coarse and fine fractions, with the Aurora 4000 sampling $PM_{10}$ particles and the Aurora 3000, located downstream of a $PM_1$ cyclone, targeting the finer fraction. Only the $PM_{10}$ dataset is considered in the present work. Instrument performances were monitored through daily zero measurements carried out with particle-free air to account for variability in gas-phase scattering contributions, such as those related to nitrogen dioxide. Calibration procedures were conducted periodically using carbon dioxide. Finally, the raw scattering data were corrected to account for known instrumental limitations, including angular truncation and non-ideal illumination, following the approach described by Müller et al. (2009).

### 2.1.2 Boundary layer profiling

The microwave profiler RPG-HATPRO G5 (MWRP G5) measures the radiation in the 20–29 and 50–59 GHz ranges emitted by the troposphere. Using a neural network (Rose et al., 2005; Löhnert and Crewell, 2003; Crewell and Löhnert, 2007) adapted to the radiometer geographic situation and trained by around 25 000 profiles, the MWRP G5 provides retrievals of tropospheric vertical profiles (0–10 km) of absolute humidity and temperature. From these data, relative humidity profiles can be calculated, as well as other thermodynamic quantities (e.g. potential temperature, liquid water content, etc). Unlike temperature and humidity, LWC is not directly retrieved from the microwave observations but is derived assuming an adiabatic thermodynamic profile for an air parcel that rises above its condensation level following the approach of Karstens et al. (1994). In this method, the adiabatic LWC profile is further empirically corrected to account for departures from adiabatic conditions, such as entrainment

and mixing. The resulting profile is then constrained to be consistent with the retrieved liquid water path (LWP) through vertical integration. The uncertainty of LWP retrievals from microwave radiometry is typically estimated to be on the order of 20–30 g m$^{-2}$ for liquid clouds (Marchand et al., 2003; Turner, 2007), although larger relative uncertainties are expected for low-LWP conditions. The uncertainty of the derived LWC profiles is more difficult to quantify, as it additionally depends on the assumptions used in the retrieval, including cloud boundary determination, adiabaticity, and the empirical correction applied to represent sub-adiabatic conditions.

The vertical resolution of the microwave profiler is approximately 30 m in the boundary layer (BL) decreasing for higher altitudes (around 100 m from the BL up to 5 km and 400 m from 5 to 10 km). The MWRP allows for the monitoring of the thermodynamic state of the atmosphere with its high temporal resolution (1 min). The profile accuracies are typically on the order of 0.7–1.8 K RMS for temperature and 0.45–0.6 g m$^{-3}$ RMS for absolute humidity, depending on altitude (Walbröl et al., 2022). Liquid water content profiles are derived from the retrieved LWP using an adiabatic-cloud assumption rather than being directly retrieved from the microwave observations. A wide variety of weather phenomena where water vapour plays an important role can therefore be measured (e.g., Louf et al., 2015; Mascaut et al. 2023a, b, 2022; Miri et al., 2024). The MWRP is also equipped with in situ sensors for ground level measurement of temperature, water vapour, pressure, wind direction and velocity.

Boundary-layer height (BLH) is retrieved from the microwave-radiometer thermodynamic profiles using the virtual potential temperature ($\theta_v$), see Eqs. (1) and (2). BLH is defined as the altitude of the minimum of $\partial\theta_v/\partial z$ above the surface within the lowest few kilometers. If $\partial\theta_v/\partial z$ has no minimum, then BLH is automatically set to zero. Similar methods have been applied to MWRP temperature profiles by Sinclair et al. (2022), Moreira et al. (2020) and Collaud Coen et al. (2014) to diagnose the BLH.

$$\theta_v = \theta\,(1 + 0.61 q_v) \tag{1}$$

$$\theta = T\left(\frac{p_0}{p}\right)^{\frac{R}{C_p}} \tag{2}$$

Where $T$ is air temperature (K), $p$ pressure (Pa), $p_0$ (equal to 1000 hPa) a reference pressure, $q_v$ the specific humidity (kg kg$^{-1}$), $R$ the gas constant for dry air (i.e. 287.05 J K$^{-1}$ kg$^{-1}$), and $C_p$ the specific thermal capacity of dry air at constant pressure (i.e. 1004 J K$^{-1}$ kg$^{-1}$).

### 2.2 Space-based cloud properties CLAAS-3

Satellite observations are used to retrieve optical properties of clouds. On the one hand, instruments on polar orbiting satellites have a better spatial resolution, e.g., about 1 km spatial resolution for cloud products from MODIS instruments for example (Platnick et al., 2003), covering the Earth surface in one day, so that only one measurement per day can be co-located with ground-based observations. On the other hand, instruments on geostationary satellites generally provide lower spatial resolution but offer a fixed viewing geometry and high temporal sampling, enabling frequent observations of the same region and facilitating the temporal co-location of satellite retrievals with ground-based measurements. The Spinning Enhanced Visible and Infrared Imager (SEVIRI), on board the geostationary METEOSAT Second Generation satellites, has a temporal resolution of 15 min and measures in four visible and near-infrared channels and eight infrared channels, with a spatial resolution of 1 km for the High-Resolution Visible (HRV) channel (broadband, 0.4–1 µm) and 3 km for the others (Schmetz et al., 2002). At the latitude and longitude of the ATOLL station, the horizontal spatial resolution of SEVIRI pixels is about $5 \times 5$ km$^2$.

The CLoud property dAtAset using SEVIRI – edition 3 (CLAAS-3, Benas et al., 2023) retrieves cloud properties based on measurements in the visible and near infrared. Cloud detection is performed using a naive Bayesian approximation. Cloud observations from the space-based Lidar CALIOP and SEVIRI reflectances were used to train the algorithm. Cloud top pressure is retrieved from a multilayer perceptron neural network trained with data from CALIOP and SEVIRI measurements in the infrared channels (3.7, 8.5, 11, and 12 µm). Cloud thermodynamic phase is inferred from an adapted algorithm described by Pavolonis et al. (2005) based on a decision tree measurement from infrared channels (3.9, 6.3, 8.7, 10.8, 12, and 13.4 µm). The algorithm retrieves six different types of clouds: liquid, supercooled, opaque ice, cirrus, overlap and overshooting. Only liquid clouds are studied here, so only the first two categories are considered. Cloud optical thickness ($\tau$) and cloud droplet effective radius ($r_e$) are determined using a look-up table following the method of Nakajima and King (1990) via a visible channel at 0.6 µm and a shortwave infrared channel at 3.9 µm. The LWP is retrieved from the cloud optical depth and $r_e$ assuming a vertically homogeneous water content, following the method from Stephens (1978). Cloud droplet number concentration ($n_d$) is also retrieved from the cloud optical depth and $r_e$ considering an idealized stratiform boundary-layer cloud following adiabaticity assumptions, with a fixed dispersion of the assumed cloud droplet size distribution (Bennartz and Rausch, 2017).

A comprehensive evaluation of CLAAS-3 is given in Benas et al. (2023), and we report here a brief summary. A comparison with CALIPSO on a $1.5° \times 1.5°$ grid for 2013 reveals differences in liquid cloud fraction of up to 30 %, but lower than 10 % over the ATOLL station. The difference is even smaller if upper clouds with $\tau$ less than 0.1 are excluded from CALIOP measurements. Note that CALIPSO serves as the reference in Benas et al. (2023), and that the reported bias encompasses all cloud types – not exclusively low-level clouds – so type-specific biases may vary due to the sensitiv-

ity of the instruments (Stubenrauch et al., 2024). Cloud optical depth, $r_e$ and $n_d$ were compared with AMSR2, MODIS, and in situ measurements. Coefficients of determination of 0.53 and 0.58 have been retrieved between $\tau$ and $r_e$ respectively from CLAAS-3 using the 3.9 µm channel and from MODIS measurements using 3.7 µm (Benas et al., 2023). Similarly, a correlation coefficient of 0.71 was retrieved between $n_d$ from CLAAS-3 and MODIS measurements.

From our filtered dataset, over the ATOLL station, the uncertainty ranges from 0.56 to 17.67 µm for $r_e$ and from 3.6 to 3276.6 $cm^{-3}$ for $n_d$, with 90 % of the dataset showing an uncertainty lower than 3.95 µm and 452.7 $cm^{-3}$ for $r_e$ and $n_d$, respectively. Lastly, it is important to acknowledge that several hypotheses and a priori assumptions in the retrieval methods could introduce uncertainties. These include (Meirink et al., 2022): (i) the assumption of plane-parallel clouds, (ii) passive satellite sensors measuring an averaged radiance of both cloudy and cloud-free areas within a pixel, (iii) surface brightness, (iv) the measured signal originating from an integrated profile, (v) LWP retrievals assuming a vertically uniform $r_e$, while $n_d$ retrievals assume an increasing $r_e$ with height, which is more representative of stratocumulus clouds, (vi) aerosols above clouds not being considered in the retrievals, and (vii) $r_e$ and $\tau$ being retrieved from look-up tables using the doubling adding Koninklijk Nederlands Meteorologisch Instituut (KNMI) method (Wolters et al., 2006), assuming liquid clouds between 1 and 2 km in height. It is also worth noting that SEVIRI requires approximately 12 min to scan the Earth's full disk from south to north, meaning that the temporal resolution, in addition to the coarse spatial resolution, may introduce further uncertainty. This effect, however, may be partially mitigated by the temporal averaging of ground-based measurements over the 15 min CLAAS-3 resolution. Spatial collocation between CLAAS-3 and the ground-based station was performed using a nearest-neighbour approach, i.e., the CLAAS-3 pixel closest to the ATOLL station location was selected, without any spatial interpolation.

## 3 Methodology

The objective of this study is to relate aerosol properties measured near the surface to cloud microphysical properties observed from space, necessarily requiring a set of physical and observational assumptions. Ground-based datasets are point measurements, whereas space-based measurements on a pixel-by-pixel basis cover a larger area. However, all ground-based datasets were temporally resampled to match the measurement frequency of the CLAAS-3 retrievals (0.0011 Hz, corresponding to 15 min intervals). As shown by Velazquez-Garcia et al. (2023) over a three-year period (2016–2019), the mean wind speed over ATOLL was approximately 3 $m\,s^{-1}$ and only rarely exceeded 5 $m\,s^{-1}$. Thus, the temporal sampling interval corresponds with an advection distance at the ground that is closely consistent with satellite-derived cloud properties averaged over a larger spatial footprint (up to 4.5 km).

The following sections describe the criteria used to filter and classify the dataset in order to identify conditions suitable for calculating the cloud property susceptibility to aerosol burden using combined ground and space-based measurements of aerosols and clouds. Specifically, we select cases: (i) where the observed cloud base height is within the BL, suggesting a direct coupling between surface aerosols and clouds (Sect. 3.1), (ii) where the lower atmosphere is thermodynamically stable, favouring persistent low-level clouds and reducing dynamic variability (Sect. 3.2) and (iii) where the relative error of LWP measured by both the radiometer and satellite is below 60 % (empirical value) determined to retain a sufficiently large dataset while indicating that the scenes observed by both platforms are similar (Sect. 3.3) and (iv) where aerosol scattering exhibits a strong correlation with proxies for cloud condensation nuclei (CCN) (Sect. 3.4). Each criterion was applied independently to the complete dataset to quantify its individual effect on the available sample and to identify the most restrictive selection criteria. This approach was adopted to assess separately the impact of each physical constraint – cloud-type selection, boundary layer height, and satellite–ground consistency – without conflating their respective effects. Independent filtering thus provides a transparent assessment of the sensitivity of the resulting dataset to each selection criterion and the underlying physical assumptions. Once the individual impact of each criterion has been assessed, all filters are applied simultaneously to define the final dataset retained for the subsequent analysis. This resulting dataset constitutes the observational basis for the investigation presented in this study.

### 3.1 Low altitude cloud criteria

Our analysis focuses exclusively on aerosol measurements within the BLH, and we restrict our analysis to cases where the clouds are embedded within it. To identify such conditions, we use ground-based MWRP observations to determine the height of the boundary layer (e.g. Sinclair et al., 2022). Cloud base and top heights are inferred from MWRP-derived LWC profiles, with a threshold of 0.01 $g\,m^{-3}$ for cloud detection. To isolate shallow boundary-layer clouds, we applied a set of complementary filtering criteria. Only clouds with a LWP below 200 $g\,m^{-2}$ (Pruppacher and Klett, 2010), a cloud base located above 100 m and below the estimated boundary-layer height, and a cloud geometric thickness smaller than 1 km were retained. These criteria are applied jointly to select shallow clouds while minimizing the influence of fog, free-tropospheric clouds and deep convective systems. Applying this criterion reduces the dataset to 19 % of the original dataset consisting of valid data in which

all instruments (SMPS, Nephelometer, MWRP and SEVIRI) simultaneously provide valid data.

### 3.2 Atmospheric stability criteria

Atmospheric dynamics play a critical role in cloud formation and evolution (Klein and Hartmann, 1993). To isolate the influence of aerosols on cloud microphysics, we restrict our analysis to meteorologically stable conditions (Coopman et al., 2018). Atmospheric stability was assessed using temperature and humidity profiles derived from ground-based MWRP observations, combined with surface measurements to compute the equivalent potential temperature ($\theta_e$) at both the surface and the top of the cloud layer. The vertical gradient of $\theta_e$ ($d\theta_e/dz$) – calculated as the difference between these two levels – served as an indicator of moist stability. Only cases with positive gradients, indicative of thermodynamically stable stratification with respect to a saturated adiabat, were retained for further analysis. Additionally, to ensure that only shallow clouds were included, we excluded all clouds with a geometric thickness greater than 1 km, effectively filtering out cumulus clouds. This approach minimises the influence of convective mixing and dynamic lifting on cloud development. Moreover, we only retained cases with a boundary layer height (BLH) larger than 500 m to ensure a robust and reliable estimation of the boundary layer structure, avoiding situations where very shallow BLH retrievals are uncertain. Applying these stability filters independently reduced the dataset to approximately 40 % of its original size. Only cases with positive gradients, indicative of thermodynamically stable stratification with respect to a saturated adiabat, were retained for further analysis. By selecting cases that were convectively stable, and additionally excluding all clouds with a geometric thickness greater than 1 km, it is assumed that cumuliform clouds are removed from the sample.

### 3.3 Similar scenes

To ensure consistency between ground-based (MWRP) and satellite (CLAAS-3) liquid water path (LWP) retrievals, we applied a 60 % relative difference threshold as an empirical filter. This threshold was selected pragmatically to retain more than 50 % of the available cases while reducing observations for which the two independent measurements disagree substantially, likely because they sample different cloud scenes (e.g., due to horizontal displacement or vertically heterogeneous cloud structures). When applied independently, this filter removes approximately 45 % of the original dataset.

### 3.4 Cloud condensation nuclei criteria

Aerosol properties measured at the surface are used as a proxy for the aerosol population interacting with the cloud base. This assumption is made for practical reasons, as direct observations at cloud base are not available. When the boundary layer is more stable, it is reasonable to anticipate a difference between aerosol concentrations measured at the surface and those at the cloud base. However, since cloud susceptibilities to aerosol burden is quantified in terms of relative changes, the metric is relatively insensitive to absolute differences in aerosol concentration: changes in surface aerosol concentrations are assumed to scale proportionately with changes at cloud base.

CCN are not directly measured at ATOLL. Fine aerosols (with diameters $D_p$ less than 100 nm) are generally inefficient both in acting as CCN and in scattering light (Dusek et al., 2006). Figure 2 compares the aerosol number concentration (CN) and $\sigma_{sp}$ data between 2020 and 2024 when the dataset is constrained or not for CCN. The highest aerosol concentrations were typically observed during the summer months, coinciding with the peak frequency of new particle formation events (Crumeyrolle et al., 2023). During these periods, CN concentrations often reached values larger than 10 000 $cm^{-3}$. A threshold for the effective radius (greater than 39 nm) calculated from the SMPS size distribution measurements was used to remove cases when aerosols are too small to serve as CCN (Garrett et al., 2004). Using this threshold allows the maximisation of the correlation coefficient (from 0.13 to 0.35) between CN and $\sigma_{sp}$ and the retention of 20 % of the initial database (Table 2).

When applied individually to the dataset, low cloud altitude, atmospheric stability, similar scenes and the CCN criteria retained 19 %, 40 %, 45 % and 20 % of the total cases, respectively (see Table 2). However, when applied simultaneously, only 3 % of the original dataset (201 out of 8019 cases) remained. Assuming the four criteria were statistically independent, we would expect less than 1 % of the dataset to satisfy all four criteria simultaneously. The much larger observed overlap (3 %) indicates that those criteria are not fully independent and may overlap more than expected, meaning some cases simultaneously satisfy multiple conditions more often than random chance would predict. While this stringent filtering reduces the dataset to only 3 % of the original cases, it improves the physical consistency of the selected cases and ensures that retained cases are representative of the targeted regime. Although this drastic reduction in sample size is a limitation of the method, it is the necessary trade-off for obtaining a physically consistent dataset. These selected data points represent situations with minimal uncertainty in cloud-aerosol attribution and meet all requirements in terms of temporal and spatial collocation, cloud type, aerosols and boundary layer conditions. Therefore, despite their limited number, these cases provide a robust and representative basis for our analysis.

Figure 3 presents a climatology of $r_e$, $n_d$, CN, $\sigma_{sp,525\,nm}$, and $d\theta_e/dz$, alongside the number of data points retained after applying the constraints. Following the filtering process, 31 % of all data points are observed during winter, while only 13 % are observed during summer. This disparity primarily stems from the stability filter: since $d\theta/dz$ is typi-

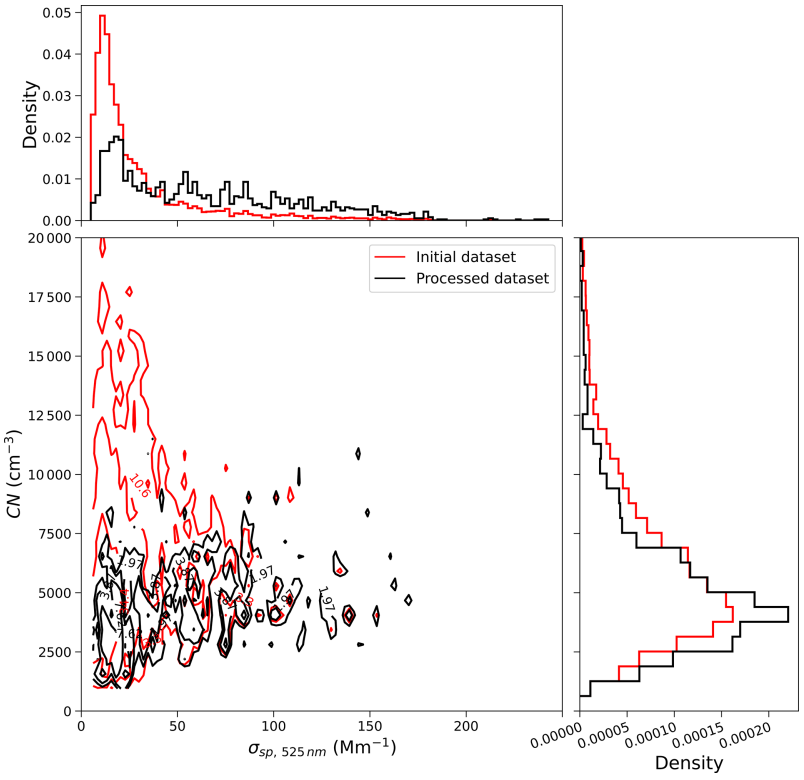



**Figure 2.** A 2-D histogram of the aerosol number concentrations (CN) and dried aerosol light scattering ($\sigma_{\mathrm{sp,525\,nm}}$) measured at ATOLL from 2020 to 2024 when the dataset is not constrained (in red) and when only particles with a diameter larger than 39 nm are kept, CCN criterion (in black) following Garrett et al. (2004). The histograms on the right and on the top are the normalized histograms of CN and $\sigma_{\mathrm{sp,525\,nm}}$ respectively when the dataset is not constrained (in red) and when the CCN criteria is applied (in black).

**Table 2.** Number of valid data points retained for the study. Initial database corresponds to cases when CLAAS3 and ground based in situ/remote sensing instruments are simultaneously available (8019). The low altitude cloud, atmospheric stability, similar scenes and CCN criteria were then applied individually and simultaneously (All combined) to the initial database.

| | Initial database | Low altitude cloud | Atmospheric Stability | Similar scenes | CCN | All combined |
|---|---|---|---|---|---|---|
| Number | 8019 | 1501 | 3321 | 3590 | 1570 | 201 |
| Percentage | 100 % | 19 % | 40 % | 45 % | 20 % | 3 % |

cally higher in winter, more data points meet the criteria during this season. For the cloud parameters, no distinct seasonal trends emerge; instead, they exhibit relative constancy throughout the year. Indeed, $r_{\mathrm{e}}$ and $n_{\mathrm{d}}$ unconstrained climatologies (Fig. S1 in the Supplement) are similar to the constrained ones (Fig. 3). While the year 2023 accounts for a larger fraction of the filtered dataset ($\sim$ 44 %), most retrieved parameters do not show strong variations across years, with the exception of a slight increase in droplet size in 2023, whose origin remains unclear (cf. Fig. S2).

## 4 Preliminary results and Discussions

In this section, the cloud droplet number and effective radius susceptibilities to aerosol loadings are estimated. Although dividing the dataset into LWP classes reduces the number of observations available in each subset, this stratification is essential in aerosol-cloud interaction studies. LWP is a key controlling variable, and the classical Twomey and Albrecht effects are generally evaluated under approximately constant LWP conditions to minimize the influence of cloud macrophysical variability on cloud microphysical properties. Moreover, several studies have shown that aerosol-cloud susceptibilities strongly depend on LWP. In particular, Zheng et al. (2020) reported systematic variations in cloud susceptibil-

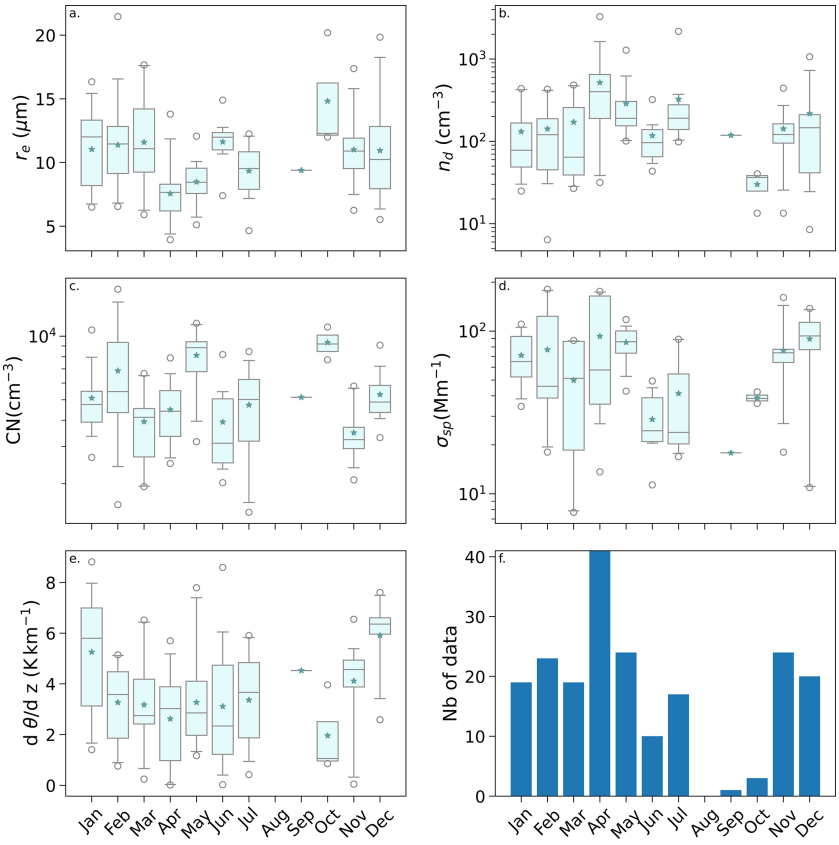



**Figure 3.** Climatologies of **(a)** cloud droplet effective radius ($r_e$), **(b)** cloud droplet number concentration ($n_d$), **(c)** particle concentration (CN), **(d)** dried aerosol light scattering ($\sigma_{sp,525\,nm}$), **(e)** potential temperature vertical gradient ($d\theta/dz$), and **(f)** the number of observations (Nb of data) over the ATOLL station when all filters described in Sect. 3 are applied. For panels **(a)** to **(e)**, the box represents the interquartile range (25th–75th percentiles), with the median indicated by a horizontal line and the mean by the star. Whiskers extend to the 1st and 99th percentiles and outliers of the whiskers are shown as individual points.

ity across different LWP regimes. Consequently, separating the analysis by LWP provides a more physically meaningful interpretation of the retrieved susceptibilities, despite the reduction in sample size.

### 4.1 Cloud droplet number concentration

The relationships between the $n_d$ and $r_e$ and the aerosol scattering coefficient ($\sigma_{sp,525\,nm}$) are illustrated in Figs. 4 and 5, respectively, for two ranges of LWP derived from the MWRP observations: from 20 to 100 and from 100 to 200 g m$^{-2}$. We observe that $n_d$ increases with $\sigma_{sp,525\,nm}$ for both LWP ranges. For low LWP, $n_d$ values rise from 58 cm$^{-3}$ at a scattering coefficient around 8.0 Mm$^{-1}$ to 205 cm$^{-3}$ around 180 Mm$^{-1}$. For larger LWP values, $n_d$ values rise from 96 cm$^{-3}$ at a scattering coefficient around 8 Mm$^{-1}$ to 269 cm$^{-3}$ at 170.0 Mm$^{-1}$. This observation aligns with previous studies that have explored the relationship between aerosol scattering properties and droplet formation. Under the ACTRIS dry-sampling conditions, higher scattering coefficients reflect increased aerosol loading and/or changes in aerosol size distribution. For example, Garrett et al. (2004) demonstrated that higher scattering coefficients are often associated with greater number of droplets. Similarly, MacDonald et al. (2020) and Motos et al. (2023) reported that enhanced scattering can result from either increased aerosol number concentrations, a shift toward larger particle sizes, or a combination of both, which contribute to increased droplet nucleation rates.

The cloud droplet concentration susceptibility to aerosol scattering coefficient, or nucleation efficiency ($S_n$), is defined as:

$$S_n = \frac{d\ln(n_d)}{d\ln(\sigma_{sp})} \quad (3)$$

To assess the uncertainty associated with the linear regression slope in log-log space, we calculated the standard error of the slope based on the residual variance and the spread of the independent variable, and derived a 95 % confidence interval. This interval provides a statistically robust range within which the true slope is expected to lie, thus offering a quantitative estimate of regression uncertainty. Over the pe-

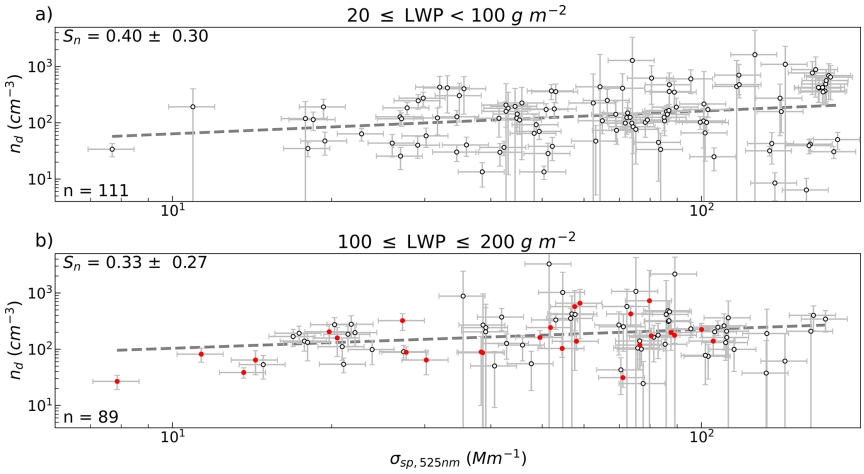



**Figure 4.** Retrievals of cloud droplet number concentration ($n_d$) versus surface measurements of light scattering by dried haze aerosol $\sigma_{sp,525\,nm}$ when the dataset is constrained for $20 < LWP < 100\,g\,m^{-2}$ **(a)** and for $100 < LWP < 200\,g\,m^{-2}$ **(b)**. The red circles represent cases with $LWP > 150\,g\,m^{-2}$. The "nucleation efficiency" $S_n$ is described by Eq. (3) and the uncertainty is derived from the 95 % confidence interval of the linear fit. $n$ represents the numbers of data points used to draw each figure.

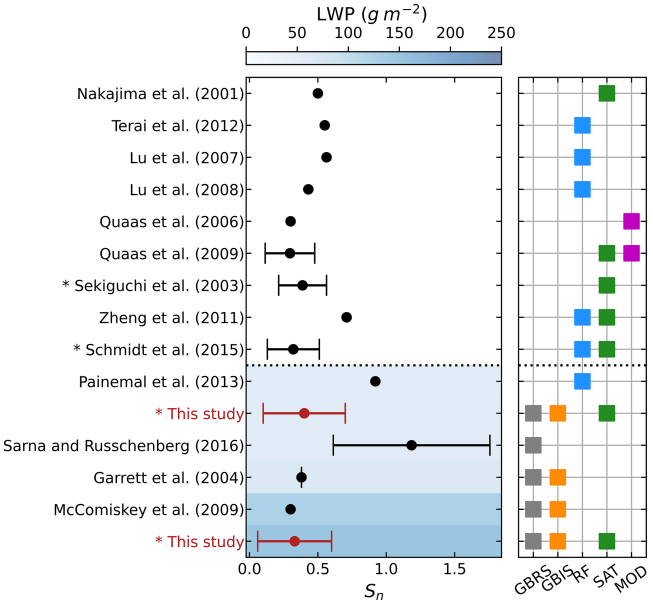



**Figure 5.** $S_n$ derived from a combination of either ground-based measurements (in-situ: orange squares; remote sensing: grey squares), airborne measurements (blue squares), satellite retrievals, and/or simulation results (purple square). The white-to-blue shaded area represents the mean liquid water path (LWP) range covered across all studies. Stars indicate studies that directly reported uncertainties in their analysis, while for the remaining studies, uncertainties were recalculated using author-provided datasets for different case studies (e.g., regions or seasons) or different models. The red color corresponds to our study. GBRS and GBIS stand for Ground Based Remote Sensing and In-Situ, RF for Research Flight, SAT for satellite, MOD for model.

riod of interest, we find that the cloud droplet concentration susceptibility ($S_n$) is ranging from $0.40 \pm 0.30$ for LWP between 20 and 100 g m$^{-2}$ to $0.33 \pm 0.27$ for LWP between 100 and 200 g m$^{-2}$. When defined as the ratio of cloud droplet number concentration to CCN number concentration, the activation fraction is physically bounded by unity, as the number of activated droplets cannot exceed the available CCN. However, in this study, aerosol loading is characterized by the aerosol scattering coefficient rather than by CCN number concentration. As an optical proxy for aerosol loading, the scattering coefficient does not represent a particle number concentration and therefore does not impose an upper bound of unity on the resulting ratio. Consequently, values greater than 1 are physically possible within the formulation adopted here and should not be interpreted as indicative of an error in the calculation.

Often, observations above 150 g m$^{-2}$ are excluded from consideration to avoid precipitating clouds (McComiskey et al., 2009). As these cases do not impose any constraint on the fit, either upward or downward, we choose to keep such cases due to the low number of data points but those observations are highlighted (red dots) in Figs. 4 and 5. Generally, as expected, an increased aerosol loading leads to higher cloud droplet concentrations.

These results are comparable in magnitude to those reported in the literature (Fig. 5). At least 9 studies reported in Fig. 5 do not provide LWP range using a combination of either airborne measurement, satellite and simulation (Nakajima et al., 2001; Terai et al., 2012; Lu et al., 2008, 2007; Quaas et al., 2006, 2009; Sekiguchi et al., 2003; Zheng et al., 2011, Schmidt et al., 2015). They reported $S_n$ values from 0.078 to 0.787. Sarna and Russchenberg (2016), using ground-based remote sensing retrievals of droplet number

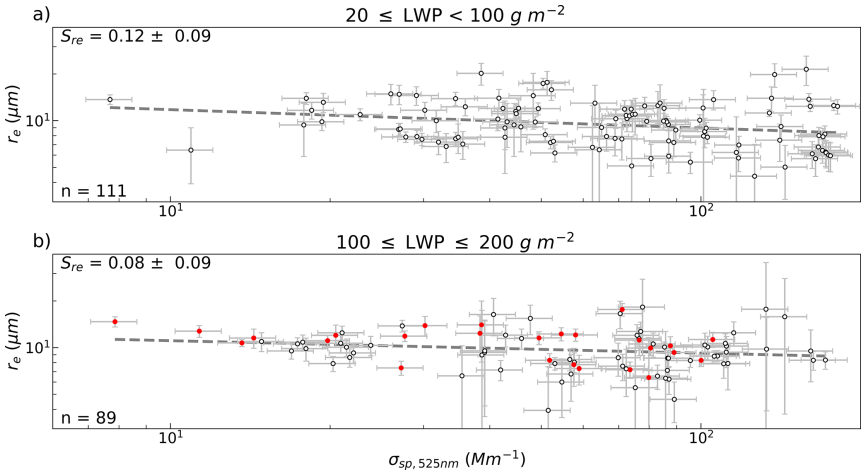



**Figure 6.** Retrievals of cloud effective radius ($r_e$) versus surface measurements of light scattering by dried haze aerosol $\sigma_{sp,525\,nm}$ when the dataset is constrained for $20 < LWP < 100\,g\,m^{-2}$ **(a)** and for $100 < LWP < 200\,g\,m^{-2}$. The red circles represent cases with $LWP > 150\,g\,m^{-2}$. The aerosol cloud-droplet-size interaction parameter $S_{re}$ is described by Eq. (4). The data are sorted according to the magnitude of cloud LWP. *n* represents the numbers of data points used to draw each figure.

concentration and integrated attenuated backscatter, found $S_n$ values between 0.78 and 1.59 for two case studies with LWP between 30 and 90 g m$^{-2}$. Furthermore, Painemal and Zuidema (2013) reported a $S_n$ of 0.92 in a range of LWP centered at 55 g m$^{-2}$ using onboard in-situ instruments. In a larger statistical analysis, McComiskey et al. (2009) reported substantially lower $S_n$ values, ranging from 0.51 to 0.64 for LWP between 107 and 143 g m$^{-2}$, using MWRP-derived $n_d$ and aerosol light scattering from a nephelometer.

### 4.2 Cloud droplet effective radius

As was done for the $n_d$ analysis, $r_e$ is plotted as a function of the aerosol scattering coefficient ($\sigma_{sp,525\,nm}$) as shown in Fig. 6, showing that $r_e$ decreases as the scattering coefficient increases: considering the linear fit function, for a scattering coefficient of 8 Mm$^{-1}$, the median $r_e$ is 12 µm, whereas for 180 Mm$^{-1}$ it is 8.4 µm for low LWP. This trend indicates that increased aerosol scattering is associated with smaller cloud droplet sizes. For large LWP values, the median $r_e$ is 11.3 µm when the scattering coefficient is around 8 Mm$^{-1}$, whereas for 170 Mm$^{-1}$ it is about 8.8 µm. The $S_{re}$, relating the droplet effective radius susceptibility to the aerosol burden, is defined as:

$$S_{re} = -\frac{d\ln(r_e)}{d\ln(\sigma_{sp})} \quad (4)$$

Since $r_e$ depends on LWP, Eq. (4) should ideally be evaluated for a fixed LWP value as suggested by Feingold (2003). Over Lille, the $S_{re}$ lies between the reported values with $0.12 \pm 0.09$ and $0.08 \pm 0.09$ for low and high LWP ranges, respectively. The uncertainties were assessed similarly to those for $S_n$ using a 95 % confidence interval. This observation is consistent with established research on $S_{re}$, which suggests that higher aerosol concentrations lead to a greater number of smaller droplets due to increased competition for available water vapor (McComiskey et al., 2009; Feingold, 2003).

Figure 7 presents previously reported values of $S_{re}$ derived from a combination of ground-based observations (in situ and remote sensing), airborne measurements, satellite retrievals, and/or numerical simulations. The results from this study (red symbol) are comparable in magnitude to those reported in the literature. Higher $S_{re}$ values (0.15–0.33) are generally found in studies where the LWP range was not constrained (Feingold et al., 2001; Twohy et al., 2005; Lu et al., 2008; Costantino and Bréon, 2013). Feingold et al. (2001) and Twohy et al. (2005) reported the highest retrieved $S_{re}$ values, ranging from 0.12–0.38 and 0.307–0.332, respectively. The elevated $S_{re}$ values reported by Feingold et al. (2001) may be attributed to smoke-affected conditions over Brazil, whereas those reported by Twohy et al. (2005) may reflect the limited sample size (only 16 observations) and the use of aerosol number concentration measurements rather than aerosol optical properties. For low LWP conditions (below 100 g m$^{-2}$), Sarna and Russchenberg (2016) reported $S_{re}$ values ranging from 0.00 to 0.09, in good agreement with our findings. In contrast, Garrett et al. (2004) retrieved a higher $S_{re}$ value of 0.17 over the Arctic, suggesting that aerosol-cloud interactions may vary depending on the environmental conditions in which the observations are made. For higher LWP conditions (above 150 g m$^{-2}$), reported $S_{re}$ values typically range between 0.02 and 0.17 (Feingold, 2003; Kim et al., 2008), which encompasses the values obtained in the present study. Interestingly, based on cloud-radar estimates of $r_e$ and Raman lidar aerosol extinction, Feingold (2003) derived $S_{re}$ values averaged at $0.1 \pm 0.04$ from seven cases

(ranging from 0.02 to 0.16) observed at the DOE ARM Southern Great Plains site in Oklahoma. Using the same methodology at the same site, Kim et al. (2008) reported comparable $S_{re}$ values (0.04–0.17) from a three-year dataset of continental stratus clouds. This close agreement suggests that, when the retrieval methodology and observational setting are consistent, the number of observations alone may not substantially influence the retrieved $S_{re}$ values.

For both $n_d$ and $r_e$, the susceptibility uncertainties are larger than the susceptibility values themselves. To evaluate the robustness of our results, we performed a sensitivity analysis by randomly excluding 25 % of the dataset 1000 times and recalculating $S_n$ and $S_{re}$ for each realization. The mean retrieved $S_{re}$ values were 0.12 and 0.08 for the low and high LWP ranges, respectively, while the corresponding mean $S_n$ values were 0.41 and 0.33 (see Fig. S3). These results indicate that our analysis is robust to random reductions in the dataset, despite its limited size. Increasing the number of data points, by including additional ACTRIS sites, for example, may substantially reduce uncertainties or permit increasing the number of LWP bins. Zheng et al. (2020) were able to estimate cloud effective radius susceptibilities for 6 LWP bins using ground-based measurements alone, and show that susceptibility tends to be largest for smaller LWP values.

## 5 Conclusions

Our results show how cloud droplet concentration and effective radius susceptibilities can be evaluated by combining ground-based measurements of aerosols with satellite retrievals of cloud microphysics. The methodology describes different criteria used to compare aerosol properties measured (aerosol scattering coefficient) at the ground with cloud properties ($r_e$, $n_d$) retrievals from satellite observations. From 5 years of data, cases were analysed where (1) the cloud base height is within the BL height, (2) the atmosphere is convectively stable, (3) cloud scenes are similar and finally (4) aerosols are large enough to act as CCN. For this subset, we observed as expected that the cloud droplet effective radius decreased and the cloud droplet number concentration increased as aerosol loading increased. More interestingly, the cloud droplet concentration susceptibility to aerosol scattering coefficient ($S_n$) was estimated at 0.40 and 0.33 for both LWP bins (above and below 100 g m$^{-2}$) while the cloud droplet effective radius susceptibility to aerosol loading ($S_{re}$) remained below 0.12 for both LWP bins. These findings underscore the critical role of aerosols in modulating cloud properties and, consequently, their impact on climate systems. However, the limited availability of data has restricted our ability to achieve statistically robust results and to apply additional criteria on aerosol chemical composition for example.

An inevitable limitation of our study is that satellite observations have coarser resolution than ground-based observations which affects the quantification of cloud susceptibilities to aerosol loading (McComiskey and Feingold, 2012). However, the baseline uncertainty associated with any individual approach remains high. For example, Jia et al. (2021) argued that studies based on satellite observations can underestimate the susceptibilities by 55 % compared to studies based on

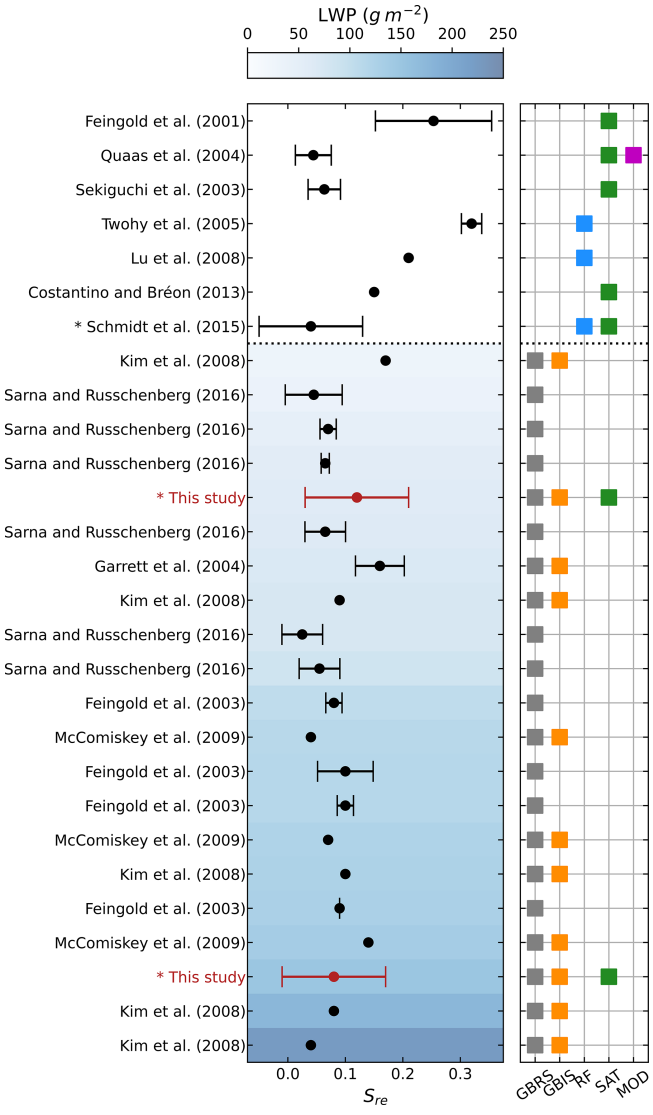



**Figure 7.** $S_{re}$ derived from a combination of either ground-based measurements (in-situ: orange squares; remote sensing: grey squares), airborne measurements (blue squares), satellite retrievals, and/or simulation results (purple square). The white-to-blue shaded area represents the mean liquid water path (LWP) range covered across all studies. Stars indicate studies that directly reported uncertainties in their analysis, while for the remaining studies, uncertainties were recalculated using author-provided datasets for different case studies (e.g., regions or seasons) or different models. The red color corresponds to our study. GBRS and GBIS stand for Ground Based Remote Sensing and In-Situ, RF for Research Flight, SAT for satellite, MOD for model.

ground-based stations. While this study is based on a single ACTRIS site in northern France (ATOLL), the methodology is readily extendable to other stations within the ACTRIS network. Many of these sites operate high-quality in-situ aerosol instrumentation and are increasingly collocated with remote sensing facilities capable of characterizing cloud properties. Sites such as SIRTA (Paris, France), Hyytiala (Finland) or Cabauw (Netherland) span a variety of aerosol and meteorological regimes – from clean continental to polluted boundary layers. Expanding the methodology to a coordinated subset of ACTRIS stations would not only allow for a systematic assessment of regional contrasts in aerosol-cloud interactions, but also increase the statistical robustness of the observed relationships. Furthermore, the integration of collocated aerosol chemical composition measurements – mass spectrometry or filter-based analyses for example – would enable a more refined constraint on cloud microphysical responses and help disentangle the influence of aerosol hygroscopicity and mixing state (Zhang and Jimenez, 2015).

*Data availability.* ATOLL in-situ measurements are available through the EBAS database (https://ebas.nilu.no/, last access: 9 October 2026) and SMPS data before 2020 through https://doi.org/10.5281/zenodo.6794562 (Crumeyrolle, 2022; Crumeyrolle et al., 2023). The CLAAS-3 data set can be found online (https://doi.org/10.5676/EUM_SAF_CM/CLAAS/V003, Meirink et al., 2022).

*Supplement.* The supplement related to this article is available online at https://doi.org/10.5194/amt-19-7097-2026-supplement.

*Author contributions.* SC, QC and TG jointly designed the study. Data analysis and the construction of figures were made by SC and QC. EB ensure that all ATOLL instruments are working properly, SC reviewed the quality of in-situ data and OP the MWRP data. All authors were involved in drafting and reviewing the manuscript.

*Competing interests.* The contact author has declared that none of the authors has any competing interests.

*Disclaimer.* Publisher's note: Copernicus Publications remains neutral with regard to jurisdictional claims made in the text, published maps, institutional affiliations, or any other geographical representation in this paper. The authors bear the ultimate responsibility for providing appropriate place names. Views expressed in the text are those of the authors and do not necessarily reflect the views of the publisher.

*Acknowledgements.* Part of the instrumental system has been financially supported by the French national research agency (ANR) under the MABCaM (ANR-16-CE04-0009) contract and by the CaPPA project (Chemical and Physical Properties of the Atmosphere), which is funded by the French National Research Agency (ANR) through the PIA (Programme d'Investissement d'Avenir) under contract "ANR-11-LABX-0005-01", and by the Regional Council "Hauts-de-France". ATOLL is a French component of the Aerosol, Clouds and Trace Gases Research Infrastructure (ACTRIS, https://www.actris.eu/). The authors also thank the Région Hauts-de-France, the Ministère de l'Enseignement Supérieur et de la Recherche (CPER Climibio). The work performed was done (i.a.) by using data from EUMETSAT's Satellite Application Facility on Climate Monitoring (CM SAF) CLAAS-3.

*Financial support.* This work was partly supported by the French National Research Agency (ANR) through the Chaire de Professeur Junior (CPJ) program, grant ANR-23-CPJ-0045-0. The French State under the France-2030 program and the initiative of the Excellence of the University of Lille are acknowledged for the funding and support granted to the R-CDP-24-003-AREA project.

*Review statement.* This paper was edited by Piet Stammes and reviewed by two anonymous referees.

## References

Bellouin, N., Quaas, J., Gryspeerdt, E., Kinne, S., Stier, P., Watson-Parris, D., Boucher, O., Carslaw, K. S., Christensen, M., Daniau, A. L., Dufresne, J. L., Feingold, G., Fiedler, S., Forster, P., Gettelman, A., Haywood, J. M., Lohmann, U., Malavelle, F., Mauritsen, T., McCoy, D. T., Myhre, G., Mülmenstädt, J., Neubauer, D., Possner, A., Rugenstein, M., Sato, Y., Schulz, M., Schwartz, S. E., Sourdeval, O., Storelvmo, T., Toll, V., Winker, D., and Stevens, B.: Bounding Global Aerosol Radiative Forcing of Climate Change, Rev. Geophys., 58, e2019RG000660, https://doi.org/10.1029/2019RG000660, 2020.

Benas, N., Solodovnik, I., Stengel, M., Hüser, I., Karlsson, K.-G., Håkansson, N., Johansson, E., Eliasson, S., Schröder, M., Hollmann, R., and Meirink, J. F.: CLAAS-3: the third edition of the CM SAF cloud data record based on SEVIRI observations, Earth Syst. Sci. Data, 15, 5153–5170, https://doi.org/10.5194/essd-15-5153-2023, 2023.

Bennartz, R. and Rausch, J.: Global and regional estimates of warm cloud droplet number concentration based on 13 years of AQUA-MODIS observations, Atmos. Chem. Phys., 17, 9815–9836, https://doi.org/10.5194/acp-17-9815-2017, 2017.

Boichu, M., Favez, O., Riffault, V., Petit, J.-E., Zhang, Y., Brogniez, C., Sciare, J., Chiapello, I., Clarisse, L., Zhang, S., Pujol-Söhne, N., Tison, E., Delbarre, H., and Goloub, P.: Large-scale particulate air pollution and chemical fingerprint of volcanic sulfate aerosols from the 2014–2015 Holuhraun flood lava eruption of Bárðarbunga volcano (Iceland), Atmos. Chem. Phys., 19, 14253–14287, https://doi.org/10.5194/acp-19-14253-2019, 2019.

Boucher, O., Randall, D., Artaxo, P., Bretherton, C., Feingold, G., Forster, P. M., Kerminen, V.-M., Kondo, Y., Liao, H., Lohmann, U., Rasch, P., Satheesh, S. K., Sherwood, S., Stevens, B., and Zhang, X. Y.: Clouds and Aerosols, in: Climate Change 2013: The Physical Science Basis, in: Contribution of Work-

ing Group I to the Fifth Assessment Report of the Intergovernmental Panel on Climate Change, Cambridge University Press, https://doi.org/10.1017/CBO9781107415324.016, 2013.

Bovchaliuk, V., Goloub, P., Podvin, T., Veselovskii, I., Tanre, D., Chaikovsky, A., Dubovik, O., Mortier, A., Lopatin, A., Korenskiy, M., and Victori, S.: Comparison of aerosol properties retrieved using GARRLiC, LIRIC, and Raman algorithms applied to multi-wavelength lidar and sun/sky-photometer data, Atmos. Meas. Tech., 9, 3391–3405, https://doi.org/10.5194/amt-9-3391-2016, 2016.

Chen, G., Canonaco, F., Tobler, A., Aas, W., Alastuey, A., Allan, J., Atabakhsh, S., Aurela, M., Baltensperger, U., Bougiatioti, A., De Brito, J. F., Ceburnis, D., Chazeau, B., Chebaicheb, H., Daellenbach, K. R., Ehn, M., El Haddad, I., Eleftheriadis, K., Favez, O., Flentje, H., Font, A., Fossum, K., Freney, E., Gini, M., Green, D. C., Heikkinen, L., Herrmann, H., Kalogridis, A.-C., Keernik, H., Lhotka, R., Lin, C., Lunder, C., Maasikmets, M., Manousakas, M. I., Marchand, N., Marin, C., Marmureanu, L., Mihalopoulos, N., Močnik, G., Nęcki, J., O'Dowd, C., Ovadnevaite, J., Peter, T., Petit, J.-E., Pikridas, M., Matthew Platt, S., Pokorná, P., Poulain, L., Priestman, M., Riffault, V., Rinaldi, M., Różański, K., Schwarz, J., Sciare, J., Simon, L., Skiba, A., Slowik, J.G., Sosedova, Y., Stavroulas, I., Styszko, K., Teinemaa, E., Timonen, H., Tremper, A., Vasilescu, J., Via, M., Vodička, P., Wiedensohler, A., Zografou, O., Cruz Minguillón, M., and Prévôt, A. S. H.: European Aerosol Phenomenology – 8: Harmonised Source Apportionment of Organic Aerosol using 22 Year-long ACSM/AMS Datasets, Environ. Int., 107325, https://doi.org/10.1016/j.envint.2022.107325, 2022.

Cimini, C., Marzano, F. S., Ciotti, P., Cimini, D., Westwater, E. R., Han, Y., Keihm, S. J., and Ware, R.: Atmospheric Microwave Radiative Models Study Based on Ground-Based Multichannel Radiometer Observations in the 20–60 GHz Band, in: Proceedings of the Fourteenth ARM Science Team Meeting Proceedings, Albuquerque, NM, USA, 22–26 March 2004, https://radiometrics.com/wp-content/uploads/2021/10/cimini-04.pdf (last access October 2026), 2004.

Collaud Coen, M., Praz, C., Haefele, A., Ruffieux, D., Kaufmann, P., and Calpini, B.: Determination and climatology of the planetary boundary layer height above the Swiss plateau by in situ and remote sensing measurements as well as by the COSMO-2 model, Atmos. Chem. Phys., 14, 13205–13221, https://doi.org/10.5194/acp-14-13205-2014, 2014.

Coopman, Q., Garrett, T. J., Finch, D. P., and Riédi, J.: High sensitivity of arctic liquid clouds to long-range anthropogenic aerosol transport, Geophys. Res. Lett., 45, 372–381, https://doi.org/10.1002/2017GL075795, 2018.

Costantino, L. and Bréon, F.-M.: Aerosol indirect effect on warm clouds over South-East Atlantic, from co-located MODIS and CALIPSO observations, Atmos. Chem. Phys., 13, 69–88, https://doi.org/10.5194/acp-13-69-2013, 2013.

Crewell, S. and Löhnert, U.: Accuracy of boundary layer temperature profiles retrieved with multifrequency, multiangle microwave radiometry, IEEE T. Geosci. Remote, 45, 2195–2201, 2007.

Crumeyrolle, S.: Data for acp-2022-436, Zenodo [data set], https://doi.org/10.5281/zenodo.6794562, 2022.

Crumeyrolle, S., Kontkanen, J. S. S., Rose, C., Velazquez Garcia, A., Bourrianne, E., Catalfamo, M., Riffault, V., Tison, E., Ferreira de Brito, J., Visez, N., Ferlay, N., Auriol, F., and Chiapello, I.: Measurement report: Atmospheric new particle formation at a peri-urban site in Lille, northern France, Atmos. Chem. Phys., 23, 183–201, https://doi.org/10.5194/acp-23-183-2023, 2023.

Duran, B. M., Wall, C. J., Lutsko, N. J., Michibata, T., Ma, P.-L., Qin, Y., Duffy, M. L., Medeiros, B., and Debolskiy, M.: A new method for diagnosing effective radiative forcing from aerosol–cloud interactions in climate models, Atmos. Chem. Phys., 25, 2123–2146, https://doi.org/10.5194/acp-25-2123-2025, 2025.

Dusek, U., Frank, G. P., Hildebrandt, L., Curtius, J., Schneider, J., Walter, S., Chand, D., Drewnick, F., Hings, S., Jung, D., Borrmann, S., and Andreae, M. O.: Size Matters More Than Chemistry for Cloud-Nucleating Ability of Aerosol Particles, Science, 312, 1375–1378, https://doi.org/10.1126/science.1125261, 2006.

Fan, J., Wang, Y., Rosenfeld, D., and Liu, X.: Review of Aerosol-Cloud Interactions: Mechanisms, Significance, and Challenges, J. Atmos. Sci., 73, 4221–4252, https://doi.org/10.1175/JAS-D-16-0037.1, 2016.

Feingold, G.: Modeling of the first indirect effect: Analysis of measurement requirements, Geophys. Res. Lett., 30, ASC 7-1–ASC 7-4, https://doi.org/10.1029/2003GL017967, 2003.

Feingold, G., Remer, L. A., Ramaprasad, J., and Kaufman, Y.: Analysis of smoke impact on clouds in Brazilian biomass burning regions: An extension of Twomey's approach, J. Geophys. Res., 106, 22907–22922, https://doi.org/10.1029/2001JD000732, 2001.

Forster, P., Storelvmo, T., Armour, K., Collins, W., Dufresne, J.-L., Frame, D., Lunt, D. J., Mauritsen, T., Palmer, M. D., Watanabe, M., Wild, M., and Zhang, H.: The Earth's Energy Budget, Climate Feedbacks, and Climate Sensitivity, in: Climate Change 2021: The Physical Science Basis. Contribution of Working Group I to the Sixth Assessment Report of the Intergovernmental Panel on Climate Change, edited by: Masson-Delmotte, V., Zhai, P., Pirani, A., Connors, S. L., Péan, C., Berger, S., Caud, N., Chen, Y., Goldfarb, L., Gomis, M. I., Huang, M., Leitzell, K., Lonnoy, E., Matthews, J. B. R., Maycock, T. K., Waterfield, T., Yelekçi, O., Yu, R., and Zhou, B., Cambridge University Press, Cambridge, United Kingdom and New York, NY, USA, 923–1054, https://doi.org/10.1017/9781009157896.009, 2021.

Garrett, T. J. and Zhao, C.: Ground-based remote sensing of thin clouds in the Arctic, Atmos. Meas. Tech., 6, 1227–1243, https://doi.org/10.5194/amt-6-1227-2013, 2013.

Garrett, T. J., Zhao, C., Dong, X., Mace, G. G., and Hobbs, P. V.: Effects of varying aerosol regimes on low-level Arctic stratus, Geophys. Res. Lett., 31, L17105, https://doi.org/10.1029/2004GL019928, 2004.

Grosvenor, D. P., Sourdeval, O., Zuidema, P., Ackerman, A., Alexandrov, M. D., Bennartz, R., Boers, R., Cairns, B., Chiu, J. C., Christensen, M., Deneke, H., Diamond, M., Feingold, G., Fridlind, A., Hünerbein, A., Knist, C., Kollias, P., Marshak, A., McCoy, D., Merk, D., Painemal, D., Rausch, J., Rosenfeld, D., Russchenberg, H., Seifert, P., Sinclair, K., Stier, P., van Diedenhoven, B., Wendisch, M., Werner, F., Wood, R., Zhang, Z., and Quaas, J.: Remote Sensing of Droplet Number Concentration in Warm Clouds: A Review of the Current State of Knowledge and Perspectives, Rev. Geophys., 56, 409–453, https://doi.org/10.1029/2017RG000593, 2018.

Gryspeerdt, E., Quaas, J., and Bellouin, N.: Constraining the aerosol influence on cloud fraction, J. Geophys. Res.-Atmos., 121, 3566–3583, https://doi.org/10.1002/2015JD023744, 2016.

Jia, H., Ma, X., Yu, F., and Quaas, J.: Significant Underestimation of Radiative Forcing by Aerosol–Cloud Interactions Derived from Satellite-Based Methods, Nat. Commun., 12, 3649, https://doi.org/10.1038/s41467-021-23888-1, 2021.

Jokinen, V. and Mäkelä, J. M.: Closed-loop arrangement with critical orifice for DMA sheath/excess flow system, J. Aerosol Sci., 28, 643–648, https://doi.org/10.1016/S0021-8502(96)00457-0, 1997.

Karstens, U., Simmer, C., and Ruprecht, E.: Remote sensing of cloud liquid water, Meteorol. Atmos. Phys., 54, 157–171, https://doi.org/10.1007/BF01030057, 1994.

Kim, G.-G., Miller, M. A., Schwartz, S. E., Liu, Y., and Min, Q.: The role of adiabaticity in the aerosol first indirect effect, J. Geophys. Res., 113, D05210, https://doi.org/10.1029/2007JD008961, 2008.

Kim, Y.-J., Kim, B.-G., Miller, M., Min, Q., and Song, C.-K.: Enhanced Aerosol-Cloud Relationships in More Stable and Adiabatic Clouds, Asia-Pac. J. Atmos. Sci., 48, 283–293, https://doi.org/10.1007/s13143-012-0028-0, 2012.

Klein, S. A. and Hartmann, D. L.: The Seasonal Cycle of Low Stratiform Clouds, J. Climate 6, 1587–1606, https://doi.org/10.1175/1520-0442(1993)006<1587:TSCOLS>2.0.CO;2, 1993.

Laj, P., Bigi, A., Rose, C., Andrews, E., Lund Myhre, C., Collaud Coen, M., Lin, Y., Wiedensohler, A., Schulz, M., Ogren, J. A., Fiebig, M., Gliß, J., Mortier, A., Pandolfi, M., Petäja, T., Kim, S.-W., Aas, W., Putaud, J.-P., Mayol-Bracero, O., Keywood, M., Labrador, L., Aalto, P., Ahlberg, E., Alados Arboledas, L., Alastuey, A., Andrade, M., Artíñano, B., Ausmeel, S., Arsov, T., Asmi, E., Backman, J., Baltensperger, U., Bastian, S., Bath, O., Beukes, J. P., Brem, B. T., Bukowiecki, N., Conil, S., Couret, C., Day, D., Dayantolis, W., Degorska, A., Eleftheriadis, K., Fetfatzis, P., Favez, O., Flentje, H., Gini, M. I., Gregorič, A., Gysel-Beer, M., Hallar, A. G., Hand, J., Hoffer, A., Hueglin, C., Hooda, R. K., Hyvärinen, A., Kalapov, I., Kalivitis, N., Kasper-Giebl, A., Kim, J. E., Kouvarakis, G., Kranjc, I., Krejci, R., Kulmala, M., Labuschagne, C., Lee, H.-J., Lihavainen, H., Lin, N.-H., Löschau, G., Luoma, K., Marinoni, A., Martins Dos Santos, S., Meinhardt, F., Merkel, M., Metzger, J.-M., Mihalopoulos, N., Nguyen, N. A., Ondracek, J., Pérez, N., Perrone, M. R., Petit, J.-E., Picard, D., Pichon, J.-M., Pont, V., Prats, N., Prenni, A., Reisen, F., Romano, S., Sellegri, K., Sharma, S., Schauer, G., Sheridan, P., Sherman, J. P., Schütze, M., Schwerin, A., Sohmer, R., Sorribas, M., Steinbacher, M., Sun, J., Titos, G., Toczko, B., Tuch, T., Tulet, P., Tunved, P., Vakkari, V., Velarde, F., Velasquez, P., Villani, P., Vratolis, S., Wang, S.-H., Weinhold, K., Weller, R., Yela, M., Yus-Diez, J., Zdimal, V., Zieger, P., and Zikova, N.: A global analysis of climate-relevant aerosol properties retrieved from the network of Global Atmosphere Watch (GAW) near-surface observatories, Atmos. Meas. Tech., 13, 4353–4392, https://doi.org/10.5194/amt-13-4353-2020, 2020.

Lihavainen, H., Kerminen, V.-M., and Remer, L. A.: Aerosol-cloud interaction determined by both in situ and satellite data over a northern high-latitude site, Atmos. Chem. Phys., 10, 10987–10995, https://doi.org/10.5194/acp-10-10987-2010, 2010.

Löhnert, U. and Crewell, S.: Accuracy of cloud liquid water path from ground-based microwave radiometry: Part I. Dependency on cloud model statistics, Radio Sci., 38, 8041, https://doi.org/10.1029/2002RS002654, 2003.

Louf, V., Pujol, O., Sauvageot, H., and Riédi, J.: Seasonal and diurnal water vapour distribution in the Sahelian area from microwave radiometric profiling observations, Q. J. Roy. Meteor. Soc., 141, 2643–2653, https://doi.org/10.1002/qj.2550, 2015.

Lu, M.-L., Conant, W. C., Jonsson, H. H., Varutbangkul, V., Flagan, R. C., and Seinfeld, J. H.: The Marine Stratus/Stratocumulus Experiment (MASE): Aerosol-cloud relationships in marine stratocumulus, J. Geophys. Res.-Atmos., 112, https://doi.org/10.1029/2006JD007985, 2007.

Lu, M.-L., Feingold, G., Jonsson, H. H., Chuang, P. Y., Gates, H., Flagan, R. C., and Seinfeld, J. H.: Aerosol-cloud relationships in continental shallow cumulus, J. Geophys. Res.-Atmos., 113, https://doi.org/10.1029/2007JD009354, 2008.

MacDonald, A. B., Hossein Mardi, A., Dadashazar, H., Azadi Aghdam, M., Crosbie, E., Jonsson, H. H., Flagan, R. C., Seinfeld, J. H., and Sorooshian, A.: On the relationship between cloud water composition and cloud droplet number concentration, Atmos. Chem. Phys., 20, 7645–7665, https://doi.org/10.5194/acp-20-7645-2020, 2020.

Madhavan, B. L., He, Y., Wu, Y., Gross, B., Moshary, F., and Ahmed, S.: Development of a Ground Based Remote Sensing Approach for Direct Evaluation of Aerosol-Cloud Interaction, Atmosphere, 3, 468–494, https://doi.org/10.3390/atmos3040468, 2012.

Marchand, R., Ackerman, T., Westwater, E. R., Clough, S. A., Cady-Pereira, K., and Liljegren, J. C.: An assessment of microwave absorption models and retrievals of cloud liquid water using clear-sky data, J. Geophys. Res., 108, 2003JD003843, https://doi.org/10.1029/2003JD003843, 2003.

Mascaut, F., Pujol, O., Verreyken, B., Peroni, R., Metzger, J. M., Blarel, L., Podvin, T., Goloub, P., Sellegri, K., Thornberry, T., Duflot, V., Tulet, P., and Brioude, J.: Aerosol characterization in an oceanic context around Reunion Island (AERO-MARINE field campaign), Atmos. Environ., 268, 118770, https://doi.org/10.1016/j.atmosenv.2021.118770, 2022.

Mascaut, F., Pujol, O., Brioude, J., Jensen, A., Lefranc, M., Evan, S., and Crumeyrolle, S.: A competition–species model for water vapour-aerosol-cloud-rain interactions, Atmos. Res., 284, 106588, https://doi.org/10.1016/j.atmosres.2022.106588, 2023a.

Mascaut, F., Pujol, O., Brioude, J., and Jensen, A.: A 2D Ising-like model for cloud field organization in pristine oceans, Eur. Phys. J. Plus, 138, 76, https://doi.org/10.1140/epjp/s13360-022-03633-3, 2023b.

McComiskey, A. and Feingold, G.: The scale problem in quantifying aerosol indirect effects, Atmos. Chem. Phys., 12, 1031–1049, https://doi.org/10.5194/acp-12-1031-2012, 2012.

McComiskey, A., Feingold, G., Frisch, A. S., Turner, D. D., Miller, M. A., Chiu, J. C., Min, Q., and Ogren, J. A.: An assessment of aerosol-cloud interactions in marine stratus clouds based on surface remote sensing, J. Geophys. Res., 114, D09203, https://doi.org/10.1029/2008JD011006, 2009.

Meirink, J. F., Karlsson, K.-G., Solodovnik, I., Hüser, I., Benas, N., Johansson, E., Håkansson, N., Stengel, M., Selbach, N., Schröder, M., and Hollmann, R.: CLAAS-3: CM SAF CLoud property dAtAset using SEVIRI – Edition 3, Satel-

lite Application Facility on Climate Monitoring [data set], https://doi.org/10.5676/EUM_SAF_CM/CLAAS/V003, 2022.

Michibata, T.: Aerosol-Cloud Interactions in the Climate System, in: Handbook of Air Quality and Climate Change, edited by: Akimoto, H. and Tanimoto, H., Springer, Singapore, https://doi.org/10.1007/978-981-15-2527-8_35-1, 2022.

Miri, R., Pujol, O., Hu, Q., Goloub, P., Veselovskii, I., Podvin, T., and Ducos, F.: Innovative aerosol hygroscopic growth study from Mie–Raman–fluorescence lidar and microwave radiometer synergy, Atmos. Meas. Tech., 17, 3367–3375, https://doi.org/10.5194/amt-17-3367-2024, 2024.

Moreira, G. D. A., Guerrero-Rascado, J. L., Bravo-Aranda, J. A., Foyo-Moreno, I., Cazorla, A., Alados, I., Lyamani, H., Landulfo, E., and Alados-Arboledas, L.: Study of the planetary boundary layer height in an urban environment using a combination of microwave radiometer and ceilometer, Atmos. Res., 240, 104932, https://doi.org/10.1016/j.atmosres.2020.104932, 2020.

Mortier, A., Goloub, P., Podvin, T., Deroo, C., Chaikovsky, A., Ajtai, N., Blarel, L., Tanre, D., and Derimian, Y.: Detection and characterization of volcanic ash plumes over Lille during the Eyjafjallajökull eruption, Atmos. Chem. Phys., 13, 3705–3720, https://doi.org/10.5194/acp-13-3705-2013, 2013.

Motos, G., Freitas, G., Georgakaki, P., Wieder, J., Li, G., Aas, W., Lunder, C., Krejci, R., Pasquier, J. T., Henneberger, J., David, R. O., Ritter, C., Mohr, C., Zieger, P., and Nenes, A.: Aerosol and dynamical contributions to cloud droplet formation in Arctic low-level clouds, Atmos. Chem. Phys., 23, 13941–13956, https://doi.org/10.5194/acp-23-13941-2023, 2023.

Müller, T., Nowak, A., Wiedensohler, A., Sheridan, P., Laborde, M., Covert, D. S., Marinoni, A., Imre, K., Henzing, B., Roger, J.-C., Santos, S. M. D., Wilhelm, R., Wang, Y.-Q., and Leeuw, G. D.: Angular Illumination and Truncation of Three Different Integrating Nephelometers: Implications for Empirical, Size-Based Corrections, Aerosol Sci. Tech., 43, 581–586, doi10.1080/02786820902798484, 2009.

Müller, T., Laborde, M., Kassell, G., and Wiedensohler, A.: Design and performance of a three-wavelength LED-based total scatter and backscatter integrating nephelometer, Atmos. Meas. Tech., 4, 1291–1303, https://doi.org/10.5194/amt-4-1291-2011, 2011.

Nandan, R., Ratnam, M. V., Kiran, V. R., and Naik, D. N.: Aerosol-cloud interaction in water clouds observed using ground-based, in-situ, and satellite-based observations over an Indian continental region, Atmos. Res., 280, 106436, https://doi.org/10.1016/j.atmosres.2022.106436 2022.

Nakajima, T. and King, M. D.: Determination of the Optical Thickness and Effective Particle Radius of Clouds from Reflected Solar Radiation Measurements. Part I: Theory, J. Atmos. Sci., 47, 1878–1893, https://doi.org/10.1175/1520-0469(1990)047<1878:DOTOTA>2.0.CO;2, 1990.

Nakajima, T., Higurashi, A., Kawamoto, K., and Penner, J. E.: A possible correlation between satellite-derived cloud and aerosol microphysical parameters, Geophys. Res. Lett., 28, 1171–1174, https://doi.org/10.1029/2000GL012186, 2001.

Painemal, D. and Zuidema, P.: The first aerosol indirect effect quantified through airborne remote sensing during VOCALS-REx, Atmos. Chem. Phys., 13, 917–931, https://doi.org/10.5194/acp-13-917-2013, 2013.

Pavolonis, M. J., Heidinger, A. K., and Uttal, T.: Daytime global cloud typing from AVHRR and VIIRS: Algorithm description, validation, and comparison, J. Appl. Meteorol., 44, 804–826, https://doi.org/10.1175/JAM2236.1, 2005.

Platnick, S., King, M. D., Ackerman, S. A., Menzel, W. P., Baum, B. A., Riédi, J. C., and Frey, R. A.: The MODIS cloud products: Algorithms and examples from Terra, IEEE T. Geosci. Remote, 41, 459–473, 2003.

Pruppacher, H. R. and Klett, J. D. (Eds.): Microstructure of Atmospheric Clouds and Precipitation, in: Microphysics of Clouds and Precipitation, Springer, Netherlands, https://doi.org/10.1007/978-0-306-48100-0_2, 2010.

Qiu, Y., Zhao, C., Guo, J., and Li, J.: 8-Year ground-based observational analysis about the seasonal variation of the aerosol-cloud droplet effective radius relationship at SGP site, Atmos. Environ., 164, 139–146, 2017.

Quaas, J., Boucher, O., and Bréon, F.-M.: Aerosol indirect effects in POLDER satellite data and the Laboratoire de Météorologie Dynamique–Zoom (LMDZ) general circulation model, J. Geophys. Res.-Atmos., 109, https://doi.org/10.1029/2003JD004317, 2004.

Quaas, J., Boucher, O., and Lohmann, U.: Constraining the total aerosol indirect effect in the LMDZ and ECHAM4 GCMs using MODIS satellite data, Atmos. Chem. Phys., 6, 947–955, https://doi.org/10.5194/acp-6-947-2006, 2006.

Quaas, J., Ming, Y., Menon, S., Takemura, T., Wang, M., Penner, J. E., Gettelman, A., Lohmann, U., Bellouin, N., Boucher, O., Sayer, A. M., Thomas, G. E., McComiskey, A., Feingold, G., Hoose, C., Kristjánsson, J. E., Liu, X., Balkanski, Y., Donner, L. J., Ginoux, P. A., Stier, P., Grandey, B., Feichter, J., Sednev, I., Bauer, S. E., Koch, D., Grainger, R. G., Kirkevåg, A., Iversen, T., Seland, Ø., Easter, R., Ghan, S. J., Rasch, P. J., Morrison, H., Lamarque, J.-F., Iacono, M. J., Kinne, S., and Schulz, M.: Aerosol indirect effects – general circulation model intercomparison and evaluation with satellite data, Atmos. Chem. Phys., 9, 8697–8717, https://doi.org/10.5194/acp-9-8697-2009, 2009.

Quaas, J., Arola, A., Cairns, B., Christensen, M., Deneke, H., Ekman, A. M. L., Feingold, G., Fridlind, A., Gryspeerdt, E., Hasekamp, O., Li, Z., Lipponen, A., Ma, P.-L., Mülmenstädt, J., Nenes, A., Penner, J. E., Rosenfeld, D., Schrödner, R., Sinclair, K., Sourdeval, O., Stier, P., Tesche, M., van Diedenhoven, B., and Wendisch, M.: Constraining the Twomey effect from satellite observations: issues and perspectives, Atmos. Chem. Phys., 20, 15079–15099, https://doi.org/10.5194/acp-20-15079-2020, 2020.

Rose, C., Collaud Coen, M., Andrews, E., Lin, Y., Bossert, I., Lund Myhre, C., Tuch, T., Wiedensohler, A., Fiebig, M., Aalto, P., Alastuey, A., Alonso-Blanco, E., Andrade, M., Artíñano, B., Arsov, T., Baltensperger, U., Bastian, S., Bath, O., Beukes, J. P., Brem, B. T., Bukowiecki, N., Casquero-Vera, J. A., Conil, S., Eleftheriadis, K., Favez, O., Flentje, H., Gini, M. I., Gómez-Moreno, F. J., Gysel-Beer, M., Hallar, A. G., Kalapov, I., Kalivitis, N., Kasper-Giebl, A., Keywood, M., Kim, J. E., Kim, S.-W., Kristensson, A., Kulmala, M., Lihavainen, H., Lin, N.-H., Lyamani, H., Marinoni, A., Martins Dos Santos, S., Mayol-Bracero, O. L., Meinhardt, F., Merkel, M., Metzger, J.-M., Mihalopoulos, N., Ondracek, J., Pandolfi, M., Pérez, N., Petäjä, T., Petit, J.-E., Picard, D., Pichon, J.-M., Pont, V., Putaud, J.-P., Reisen, F., Sellegri, K., Sharma, S., Schauer, G., Sheridan, P., Sherman, J. P., Schwerin, A., Sohmer, R., Sorribas, M., Sun, J., Tulet, P., Vakkari, V., van Zyl, P. G., Velarde, F., Villani, P., Vrato-

lis, S., Wagner, Z., Wang, S.-H., Weinhold, K., Weller, R., Yela, M., Zdimal, V., and Laj, P.: Seasonality of the particle number concentration and size distribution: a global analysis retrieved from the network of Global Atmosphere Watch (GAW) near-surface observatories, Atmos. Chem. Phys., 21, 17185–17223, https://doi.org/10.5194/acp-21-17185-2021, 2021.

Rose, T., Crewell, S., Löhnert, U., and Simmer, C.: A network suitable microwave radiometer for operational monitoring of the cloudy atmosphere, Atmos. Res., 75, 183–200, https://doi.org/10.1016/j.atmosres.2004.12.005, 2005.

Rosenfeld, D., Sherwood, S., Wood, R., and Donner, L.: Climate Effects of Aerosol-Cloud Interactions, Science, 343, 379–380, https://doi.org/10.1126/science.1247490, 2014.

Sarna, K. and Russchenberg, H. W. J.: Ground-based remote sensing scheme for monitoring aerosol–cloud interactions, Atmos. Meas. Tech., 9, 1039–1050, https://doi.org/10.5194/amt-9-1039-2016, 2016.

Schmetz, J., Pili, P., Tjemkes, S., Just, D., Kerkmann, J., Rota, S., and Ratier, A.: An introduction to Meteosat second generation (MSG), B. Am. Meteorol. Soc., 83, 977–992, https://doi.org/10.1175/BAMS-83-7-Schmetz-2, 2002.

Schmidt, J., Ansmann, A., Bühl, J., and Wandinger, U.: Strong aerosol–cloud interaction in altocumulus during updraft periods: lidar observations over central Europe, Atmos. Chem. Phys., 15, 10687–10700, https://doi.org/10.5194/acp-15-10687-2015, 2015.

Sekiguchi, M., Nakajima, T., Suzuki, K., Kawamoto, K., Higurashi, A., Rosenfeld, D., Sano, I., and Mukai, S.: A study of the direct and indirect effects of aerosols using global satellite data sets of aerosol and cloud parameters, J. Geophys. Res.-Atmos., 108, https://doi.org/10.1029/2002JD003359, 2003.

Sena, E. T., McComiskey, A., and Feingold, G.: A long-term study of aerosol–cloud interactions and their radiative effect at the Southern Great Plains using ground-based measurements, Atmos. Chem. Phys., 16, 11301–11318, https://doi.org/10.5194/acp-16-11301-2016, 2016.

Sinclair, V. A., Ritvanen, J., Urbancic, G., Erner, I., Batrak, Y., Moisseev, D., and Kurppa, M.: Boundary-layer height and surface stability at Hyytiälä, Finland, in ERA5 and observations, Atmos. Meas. Tech., 15, 3075–3103, https://doi.org/10.5194/amt-15-3075-2022, 2022.

Stephens, G. L.: Radiation Profiles in Extended Water Clouds. I: Theory, J. Atmos. Sci., 35, 2111–2122, https://doi.org/10.1175/1520-0469(1978)035<2111:RPIEWC>2.0.CO;2, 1978.

Stubenrauch, C. J., Kinne, S., Mandorli, G., Rossow, W. B., Winker, D. M., Ackerman, S. A., Chepfer, H., Di Girolamo, L., Garnier, A., Heidinger, A., Karlsson, K.-G., Meyer, K., Minnis, P., Platnick, S., Stengel, M., Sun-Mack, S., Veglio, P., Walther, A., Cai, X., Young, A. H., and Zhao, G.: Lessons Learned from the Updated GEWEX Cloud Assessment Database, Surv. Geophys., 45, 1999–2048, https://doi.org/10.1007/s10712-024-09824-0, 2024.

Terai, C. R., Wood, R., Leon, D. C., and Zuidema, P.: Does precipitation susceptibility vary with increasing cloud thickness in marine stratocumulus?, Atmos. Chem. Phys., 12, 4567–4583, https://doi.org/10.5194/acp-12-4567-2012, 2012.

Turner, D. D.: Improved ground-based liquid water path retrievals using a combined infrared and microwave approach, J. Geophys. Res.-Atmos., 112, https://doi.org/10.1029/2007JD008530, 2007.

Twohy, C. H., Petters, M. D., Snider, J. R., Stevens, B., Tahnk, W., Wetzel, M., Russell, L., and Burnet, F.: Evaluation of the aerosol indirect effect in marine stratocumulus clouds: Droplet number, size, liquid water path, and radiative impact, J. Geophys. Res.-Atmos., 110, https://doi.org/10.1029/2004JD005116, 2005.

Velazquez-Garcia, A., Crumeyrolle, S., de Brito, J. F., Tison, E., Bourrianne, E., Chiapello, I., and Riffault, V.: Deriving composition-dependent aerosol absorption, scattering and extinction mass efficiencies from multi-annual high time resolution observations in Northern France, Atmos. Environ., 298, 119613, https://doi.org/10.1016/j.atmosenv.2023.119613, 2023.

Villani, P., Picard, D., Marchand, N., and Laj, P.: Design and validation of a 6-volatility tandem differential mobility analyzer (VTDMA), Aerosol Sci. Tech., 41, 898–906, https://doi.org/10.1080/02786820701534593, 2007.

Walbröl, A., Crewell, S., Engelmann, R., Orlandi, E., Griesche, H., Radenz, M., Hofer, J., Althausen, D., Mech, M., and Ebell, K.: Atmospheric temperature, water vapour and liquid water path from two microwave radiometers during MOSAiC, Sci. Data, 9, 440, https://doi.org/10.1038/s41597-022-01504-1, 2022.

Watson-Parris, D. and Smith, C. J.: Large uncertainty in future warming due to aerosol forcing, Nat. Clim. Chang., 12, 1111–1113, https://doi.org/10.1038/s41558-022-01516-0, 2022.

Wolters, E. L. A., Roebeling, R. A., and Stammes, P.: Cloud reflectance calculations using DAK: study on required integration points, Koninklijk Nederlands Meteorologisch Instituut, http://www.knmi.nl/publications (last access: 9 October 2026), 2006.

Zhang, R. and Jimenez, J. L.: Impact of aerosol size and chemistry on cloud condensation nuclei formation: Implications for the Twomey effect, Atmos. Environ., 101, 12–19, https://doi.org/10.1016/j.atmosenv.2014.11.023, 2015.

Zheng, X., Albrecht, B., Jonsson, H. H., Khelif, D., Feingold, G., Minnis, P., Ayers, K., Chuang, P., Donaher, S., Rossiter, D., Ghate, V., Ruiz-Plancarte, J., and Sun-Mack, S.: Observations of the boundary layer, cloud, and aerosol variability in the southeast Pacific near-coastal marine stratocumulus during VOCALS-REx, Atmos. Chem. Phys., 11, 9943–9959, https://doi.org/10.5194/acp-11-9943-2011, 2011.

Zheng, X., Xi, B., Dong, X., Logan, T., Wang, Y., and Wu, P.: Investigation of aerosol–cloud interactions under different absorptive aerosol regimes using Atmospheric Radiation Measurement (ARM) southern Great Plains (SGP) ground-based measurements, Atmos. Chem. Phys., 20, 3483–3501, https://doi.org/10.5194/acp-20-3483-2020, 2020.